

# Merged amplitude encoding for Chebyshev quantum Kolmogorov–Arnold networks: trading qubits for circuit executions

Hikaru Wakaura<sup>1,\*</sup>

<sup>1</sup>*QuantScape Inc., 4-11-18, Manshon-Shimizudai, Meguro, Tokyo, 153-0064, Japan*

(Dated: March 4, 2026)

Quantum Kolmogorov–Arnold networks based on Chebyshev polynomials (CCQKAN) evaluate each edge activation function as a quantum inner product, creating a trade-off between qubit count and the number of circuit executions per forward pass. We introduce merged amplitude encoding, a technique that packs the element-wise products of all  $n$  input-edge vectors for a given output node into a single amplitude state, reducing circuit executions by a factor of  $n$  at a cost of only 1–2 additional qubits relative to the sequential baseline. The merged and original circuits compute the same mathematical quantity exactly; the open question is whether they remain equally trainable within a gradient-based optimization loop. We address this question through numerical experiments on 10 network configurations under ideal, finite-shot, and noisy simulation conditions, comparing original, parameter-transferred, and independently initialized merged circuits over 16 random seeds. Wilcoxon signed-rank tests show no significant difference between the independently initialized merged circuit and the original ( $p > 0.05$  in 28 of 30 comparisons), while parameter transfer yields significantly lower loss under ideal conditions ( $p < 0.001$  in 9 of 10 configurations). On 10-class digit classification with the  $8 \times 8$  MNIST dataset using a one-vs-all strategy, original and merged circuits achieve comparable test accuracies of 53–78% with no significant difference in any configuration. These results provide empirical evidence that merged amplitude encoding preserves trainability under the simulation conditions tested.

## I. INTRODUCTION

Quantum machine learning has advanced rapidly as one of the most promising near-term applications of quantum computers [1–3]. Variational quantum algorithms [3] and parameterized quantum circuits [4] have emerged as leading candidates for the noisy intermediate-scale quantum (NISQ) era [5], enabling hybrid quantum-classical approaches to classification, regression, and generative modeling. However, quantum neural network architectures face a fundamental trade-off between the number of qubits required and the number of circuit executions per forward pass, and achieving a favorable balance remains an open problem [6].

Kolmogorov–Arnold networks (KAN) are function approximators based on the Kolmogorov–Arnold representation theorem [7, 8], which states that any multivariate continuous function can be decomposed into compositions and sums of univariate functions. Recently, Liu et al. [9] introduced KAN as a neural network architecture in which learnable activation functions are placed on edges rather than nodes, demonstrating competitive or superior performance compared to multilayer perceptrons in terms of both accuracy and interpretability.

The quantum extension of KAN has been explored in several recent works [10, 11]. In particular, the Chebyshev-based continuous quantum KAN (CCQKAN) [12] uses Chebyshev polynomials of the first kind as the basis for edge activation functions, encoding both the basis vector  $\mathbf{T}(x)$  and the coefficient vector  $\mathbf{c}$  as quantum amplitude states and computing their

inner product via a SWAP test [13]. The CCQKAN architecture admits two extreme execution strategies for a two-layer  $[n, n, 1]$  network with Chebyshev degree  $d$ : (a) *fully parallel* evaluation, which allocates a separate qubit register to each of the  $(n^2 + n)$  edges and requires  $Q_{\text{par}} = (n^2 + n) \lceil \log_2(d + 1) \rceil$  qubits but only one circuit execution per layer; and (b) *fully sequential* evaluation, which reuses a single  $Q_{\text{seq}} = \lceil \log_2(d + 1) \rceil$ -qubit register but requires  $(n^2 + n)$  separate circuit executions. For instance, a  $[4, 4, 1]$  network with  $d = 5$  requires either 60 qubits (parallel) or 3 qubits with 20 separate circuit calls per layer (sequential).

Between these extremes, alternative encoding strategies that batch multiple edge evaluations into a single circuit may offer a more favorable trade-off. Data re-uploading circuits [6] have demonstrated that re-encoding classical data at multiple points within a single circuit can enhance expressibility; a similar principle—encoding information from multiple edges into a single quantum state—motivates the present work.

In this paper, we present merged amplitude encoding for CCQKAN. Rather than evaluating each edge independently, this technique packs the element-wise products of Chebyshev coefficient and basis vectors for all  $n$  input edges of a given output node into a single amplitude state, computing their sum in one circuit execution using  $Q_{\text{red}} = \lceil \log_2(n(d + 1)) \rceil$  qubits. Compared to the sequential baseline (which is the practically relevant alternative), the merged approach reduces circuit executions by a factor of  $n$  at the cost of only 1–2 additional qubits ( $\Delta Q = Q_{\text{red}} - Q_{\text{seq}}$ ; Table I). Since the merged encoding computes the same mathematical quantity as the original—the sum of edge activations [Eq. (9)]—the two architectures are functionally equivalent, differing only in

\* hikaruwakaura@gmail.com

how the computation is distributed across circuit executions. This mathematical equivalence does not, however, guarantee that the two circuits have identical trainability or noise sensitivity when used within an optimization loop. The main contribution of this work is to empirically establish, through systematic numerical experiments, that the merged encoding preserves trainability under both ideal and noisy conditions. We compare three circuit variants—original, reduced with parameter transfer (Red-T), and reduced with independent initialization (Red-I)—under ideal, shot-noise, and shot-plus-device-noise conditions, employing Wilcoxon signed-rank tests with 16 seeds for statistical rigor. We additionally report MNIST digit classification results—both binary (0 vs 1) and 10-class (one-vs-all)—as supplementary consistency checks on real data.

## II. BACKGROUND

### A. Kolmogorov–Arnold representation

The Kolmogorov–Arnold representation theorem [7, 8] states that any continuous function  $f : [0, 1]^n \rightarrow \mathbb{R}$  can be written as

$$f(\mathbf{x}) = \sum_{q=0}^{2n} \Phi_q \left( \sum_{p=1}^n \phi_{q,p}(x_p) \right), \quad (1)$$

where  $\phi_{q,p} : [0, 1] \rightarrow \mathbb{R}$  and  $\Phi_q : \mathbb{R} \rightarrow \mathbb{R}$  are continuous univariate functions. KAN [9] implements a practical variant of this decomposition as a layered network in which each edge carries a learnable univariate function.

### B. Chebyshev-based CCQKAN

In CCQKAN [12], each edge activation function  $\varphi(x)$  is expanded in the Chebyshev basis of degree  $d$ :

$$\varphi(x) = \sum_{k=0}^d c_k T_k(x), \quad (2)$$

where  $T_k(x)$  denotes the Chebyshev polynomial of the first kind of degree  $k$  and  $\{c_k\}_{k=0}^d$  are learnable coefficients. Evaluating Eq. (2) is equivalent to computing the inner product  $\langle \mathbf{c}, \mathbf{T}(x) \rangle$ , where  $\mathbf{c} = (c_0, \dots, c_d)^\top$  and  $\mathbf{T}(x) = (T_0(x), \dots, T_d(x))^\top$ .

In the quantum implementation, both  $\mathbf{c}$  and  $\mathbf{T}(x)$  are padded to the nearest power of two and normalized, yielding amplitude states  $|\hat{\mathbf{c}}\rangle$  and  $|\hat{\mathbf{T}}\rangle$  in  $q_e = \lceil \log_2(d+1) \rceil$ -qubit registers. The inner product is estimated via a SWAP test [13]: an ancilla qubit is prepared in  $|+\rangle$ , a controlled-SWAP is applied between the two registers, and the ancilla is measured. The probability of measuring  $|0\rangle$  on the ancilla is

$$P(0) = \frac{1 + |\langle \hat{\mathbf{c}} | \hat{\mathbf{T}} \rangle|^2}{2}, \quad (3)$$

from which  $|\langle \hat{\mathbf{c}} | \hat{\mathbf{T}} \rangle|^2$  is estimated as  $2P(0) - 1$ . The unnormalized inner product is then recovered by multiplying by  $\|\mathbf{c}\| \cdot \|\mathbf{T}(x)\|$ . When using exact statevector simulation, the overlap  $\langle \hat{\mathbf{c}} | \hat{\mathbf{T}} \rangle$  is computed directly without the SWAP test ancilla.

For a two-layer  $[n, n, 1]$  KAN, the first layer contains  $n^2$  edges and the second layer  $n$  edges, with a global function composition factor (GFCF) consisting of learnable scale  $\alpha$  and shift  $\beta$  applied to the output:  $y = \alpha \cdot y_{\text{raw}} + \beta$ . In parallel mode, the total qubit count is

$$Q_{\text{par}} = (n^2 + n) q_e = (n^2 + n) \lceil \log_2(d+1) \rceil. \quad (4)$$

The network forward pass for a  $[n, n, 1]$  architecture proceeds as follows:

1. Inputs  $\mathbf{x} \in \mathbb{R}^n$  are normalized from the data range to  $[-1, 1]$ .
2. For each hidden node  $j \in \{1, \dots, n\}$ , the hidden activation is

$$h_j = \tanh \left( \sum_{i=1}^n \varphi_{ij}(x_i) \right), \quad (5)$$

where  $\varphi_{ij}(x_i) = \sum_{k=0}^d c_{ij,k} T_k(x_i)$  is evaluated via the quantum inner product. In the original circuit, this requires  $n$  separate inner product evaluations per hidden node.

3. The output is  $y = \alpha \left( \sum_{i=1}^n \varphi_i^{(2)}(h_i) \right) + \beta$ , computed by  $n$  inner products followed by the classical GFCF.

## III. MERGED AMPLITUDE ENCODING

### A. Derivation

Consider the computation of hidden node  $j$  in the first layer. In the original architecture, each edge  $(i, j)$  computes the inner product  $\langle \hat{\mathbf{c}}_{ij}, \hat{\mathbf{T}}(x_i) \rangle$  between normalized amplitude states, then rescales by  $\|\mathbf{c}_{ij}\| \cdot \|\mathbf{T}(x_i)\|$  to recover  $\varphi_{ij}(x_i) = \sum_k c_{ij,k} T_k(x_i)$ . The hidden node activation is

$$h_j = \tanh \left( \sum_{i=1}^n \varphi_{ij}(x_i) \right) = \tanh \left( \sum_{i=1}^n \sum_{k=0}^d c_{ij,k} T_k(x_i) \right). \quad (6)$$

Rather than computing each edge’s inner product on a separate qubit register, we define a merged vector

$$\mathbf{m}_j = \bigoplus_{i=1}^n (\mathbf{c}_{ij} \odot \mathbf{T}(x_i)) \in \mathbb{R}^{n(d+1)}, \quad (7)$$

where  $\odot$  denotes element-wise (Hadamard) multiplication and  $\oplus$  denotes concatenation. The  $l$ -th component of  $\mathbf{m}_j$  is explicitly

$$[\mathbf{m}_j]_{(i-1)(d+1)+k} = c_{ij,k} T_k(x_i), \quad (8)$$

for  $i = 1, \dots, n$  and  $k = 0, \dots, d$ . The sum of all components therefore equals the desired pre-activation:

$$S_j \equiv \sum_{l=0}^{n(d+1)-1} [\mathbf{m}_j]_l = \sum_{i=1}^n \sum_{k=0}^d c_{ij,k} T_k(x_i). \quad (9)$$

To evaluate  $S_j$  quantumly, we pad  $\mathbf{m}_j$  with zeros to dimension  $D = 2^{\lceil \log_2(n(d+1)) \rceil}$  and prepare the normalized amplitude state

$$|\tilde{\mathbf{m}}_j\rangle = \frac{\mathbf{m}_j^{\text{pad}}}{\|\mathbf{m}_j^{\text{pad}}\|} = \frac{\mathbf{m}_j^{\text{pad}}}{\|\mathbf{m}_j\|}, \quad (10)$$

where the last equality holds because the zero-padded entries do not contribute to the norm. The overlap with the uniform state  $|U\rangle = D^{-1/2} \sum_{l=0}^{D-1} |l\rangle$  is

$$\begin{aligned} \langle U | \tilde{\mathbf{m}}_j \rangle &= \frac{1}{\sqrt{D}} \sum_{l=0}^{D-1} \frac{[\mathbf{m}_j^{\text{pad}}]_l}{\|\mathbf{m}_j\|} \\ &= \frac{1}{\sqrt{D} \|\mathbf{m}_j\|} \sum_{l=0}^{n(d+1)-1} [\mathbf{m}_j]_l \\ &= \frac{S_j}{\sqrt{D} \|\mathbf{m}_j\|}, \end{aligned} \quad (11)$$

and thus

$$S_j = \|\mathbf{m}_j\| \sqrt{D} \langle U | \tilde{\mathbf{m}}_j \rangle. \quad (12)$$

This identity is exact; the merged encoding introduces no approximation beyond that inherent in the amplitude encoding and inner product estimation. We emphasize that the construction above is mathematically elementary—it follows directly from the linearity of the inner product and the definition of amplitude encoding. The contribution of this work is therefore not the identity itself, but rather the systematic empirical verification that rearranging the computation in this way preserves trainability when the circuit is used within an optimization loop (Sec. V).

Since  $|U\rangle = H^{\otimes Q_{\text{red}}} |0\rangle^{\otimes Q_{\text{red}}}$  (the uniform state is prepared by applying Hadamard gates to the all-zero state), the overlap  $\langle U | \tilde{\mathbf{m}}_j \rangle$  can be evaluated without a SWAP test: one applies  $H^{\otimes Q_{\text{red}}}$  to  $|\tilde{\mathbf{m}}_j\rangle$  and measures the probability of the all-zero outcome  $|0\rangle^{\otimes Q_{\text{red}}}$ , which equals  $|\langle U | \tilde{\mathbf{m}}_j \rangle|^2$ . In ideal simulation, the overlap is computed directly from the statevector. Under shot-based simulation,  $P(0^{\otimes Q_{\text{red}}})$  is estimated by repeated measurement as in the SWAP test protocol described above. The norm  $\|\mathbf{m}_j\|$  and the dimension  $D$  are computed classically. Note that, as with the original SWAP test, this measurement yields only  $|\langle U | \tilde{\mathbf{m}}_j \rangle|^2$ ; the sign of  $S_j$  is determined by  $\text{sign}(\sum_l [\mathbf{m}_j]_l)$ , which is computed classically from the known coefficients and basis values.

The merged encoding requires

$$Q_{\text{red}} = \lceil \log_2(n(d+1)) \rceil \quad (13)$$

qubits per register.

## B. Sign recovery

Both the SWAP test and the merged overlap measurement yield only squared overlaps ( $|\langle \cdot | \cdot \rangle|^2$ ), so the sign of  $S_j$  is not directly accessible from the quantum measurement. In our simulation, the sign is computed classically as  $\text{sign}(\sum_l [\mathbf{m}_j]_l)$  from the known coefficients and basis values. On real quantum hardware, sign recovery would require an additional Hadamard test [13], which uses one ancilla qubit prepared in  $|+\rangle$  and a controlled unitary to extract the real part of the overlap. This increases the effective qubit count by one ( $Q_{\text{red}} + 1$ ) and adds  $O(Q_{\text{red}})$  controlled gates per evaluation. We emphasize that this is a limitation shared with the original CCQKAN architecture (which also requires sign recovery for the SWAP test), not specific to the merged encoding; both architectures require the same additional ancilla on hardware.

## C. Sequential qubit reuse

The  $n$  hidden nodes and the output node are computed sequentially, reusing the same  $Q_{\text{red}}$  qubits for each evaluation. The total qubit count for the full network forward pass is thus  $Q_{\text{red}}$  as given in Eq. (13) (or  $Q_{\text{red}} + 1$  including the sign-recovery ancilla), at the cost of  $n + 1$  sequential circuit evaluations (one per hidden node plus one for the output).

## D. Resource trade-off

TABLE I. Resource comparison for  $[n, n, 1]$  CCQKAN.  $Q$ : qubits;  $C$ : circuit executions per forward pass.  $\Delta Q = Q_{\text{red}} - Q_{\text{seq}}$ .

Network	$d$	$Q_{\text{par}}$	$C_{\text{par}}$	$Q_{\text{seq}}$	$C_{\text{seq}}$	$Q_{\text{red}}$	$C_{\text{red}}$	$\Delta Q$
[2, 2, 1]	2	12	1	2	6	3	3	1
[2, 2, 1]	3	12	1	2	6	3	3	1
[2, 2, 1]	4	18	1	3	6	4	3	1
[3, 3, 1]	2	24	1	2	12	4	4	2
[3, 3, 1]	3	24	1	2	12	4	4	2
[3, 3, 1]	4	36	1	3	12	4	4	1
[4, 4, 1]	2	40	1	2	20	4	5	2
[4, 4, 1]	3	40	1	2	20	4	5	2
[4, 4, 1]	4	60	1	3	20	5	5	2
[4, 4, 1]	5	60	1	3	20	5	5	2

Table I compares the three execution strategies in terms of both qubit count ( $Q$ ) and circuit execution count ( $C$ ) per forward pass. For a two-layer  $[n, n, 1]$  network:

- Parallel:  $C_{\text{par}} = 1$  (all edges evaluated simultaneously),
- Sequential:  $C_{\text{seq}} = n^2 + n$  (one circuit per edge),
- Merged:  $C_{\text{red}} = n+1$  (one circuit per output node).

The merged approach reduces circuit executions by a factor of  $n$  relative to the sequential baseline:

$$\frac{C_{\text{red}}}{C_{\text{seq}}} = \frac{n+1}{n^2+n} = \frac{1}{n}. \quad (14)$$

For a  $[4, 4, 1]$  network, this represents a  $4\times$  reduction in circuit executions (from 20 to 5).

The qubit overhead of the merged approach relative to the sequential baseline is

$$\Delta Q = Q_{\text{red}} - Q_{\text{seq}} = \lceil \log_2(n(d+1)) \rceil - \lceil \log_2(d+1) \rceil, \quad (15)$$

which grows only as  $O(\log n)$ . In all configurations studied,  $\Delta Q$  is 1–2 qubits (Table I). Whether this modest qubit overhead is worthwhile depends on the relative cost of additional qubits versus additional circuit executions on a given hardware platform; we do not attempt to resolve this hardware-dependent question here, but instead focus on establishing that the merged encoding preserves trainability.

Figure 1 visualizes this trade-off: each network configuration maps to three points in the  $(Q, C)$  plane, illustrating how the merged approach occupies an intermediate position between the parallel (low  $C$ , high  $Q$ ) and sequential (low  $Q$ , high  $C$ ) extremes.

We note that the gate complexity of amplitude encoding is an additional factor not captured by qubit count or circuit execution count alone. Generic amplitude encoding of an arbitrary  $D$ -dimensional vector requires  $O(D)$  CNOT gates [14], which for the merged state ( $D = 2^{Q_{\text{red}}}$ ) is exponential in  $Q_{\text{red}}$ . For the sequential baseline, each edge requires amplitude encoding of a  $(d+1)$ -dimensional

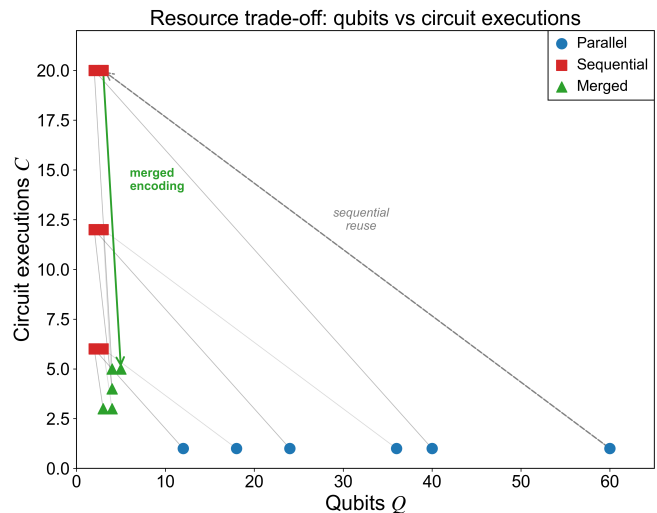


FIG. 1. Resource trade-off for all 10 configurations. Each configuration maps to three points: parallel (circle), sequential (square), merged (triangle). The merged approach reduces circuit executions  $C$  by a factor of  $n$  relative to sequential, at a cost of 1–2 additional qubits.

vector, i.e.,  $O(d)$  CNOTs per circuit execution. The merged encoding encodes an  $n(d+1)$ -dimensional vector, requiring  $O(nd)$  CNOTs per execution. Thus, while the merged approach reduces circuit executions by a factor of  $n$ , each execution uses  $O(n)$  times more gates, yielding a roughly constant total gate count. The practical advantage therefore depends on the relative cost of per-execution overhead versus per-gate noise. Specifically, the merged approach is advantageous when per-execution costs (state preparation, measurement, classical readout, and job scheduling latency) dominate over gate-level noise accumulation. This scenario arises on cloud-accessible quantum hardware where job submission latency ( $\sim$ ms per circuit) far exceeds gate times ( $\sim$  $\mu$ s), and on platforms where state preparation is the bottleneck. Conversely, on hardware where gate errors are the dominant noise source and circuit depth is the limiting

factor, the sequential baseline (which uses shallower circuits per execution) may be preferable.

### E. Parameter transfer

When transitioning from the original to the merged architecture, the Chebyshev coefficients  $\{c_{ij,k}\}$  can be directly transferred, since both architectures parameterize the same set of univariate functions. The weight tensor  $W_{ijk}^{(1)} = c_{ij,k}$  of the merged first layer is set equal to the trained coefficient of the corresponding edge in the original network; similarly for the second layer and GFCF parameters  $(\alpha, \beta)$ . This transfer provides a warm start for subsequent training. To isolate the effect of the architectural change from the initialization strategy, we study both the case with parameter transfer (Red-T) and the case with independent random initialization (Red-I).

## IV. EXPERIMENTAL SETUP

### A. Synthetic function regression

We evaluate 10 network configurations:  $[n, n, 1]$  for  $n \in \{2, 3, 4\}$  with Chebyshev degree  $d \in \{2, 3, 4\}$ , plus  $d = 5$  for  $n = 4$  (Table I). The target functions are

$$\begin{aligned} f_2(\mathbf{x}) &= \sin(x_1 + x_2), \\ f_3(\mathbf{x}) &= \sin(x_1 + x_2) + \cos(x_3), \\ f_4(\mathbf{x}) &= \sin(x_1 + x_2) + \cos(x_3 x_4). \end{aligned} \quad (16)$$

Training data consists of 30 points sampled uniformly from  $[-1, 1]^n$ , with targets normalized to  $[-2, 2]$ .

The loss function used throughout all synthetic experiments is the mean squared error (MSE):

$$\mathcal{L}(\boldsymbol{\theta}) = \frac{1}{N} \sum_{i=1}^N (\hat{y}_i(\boldsymbol{\theta}) - y_i)^2, \quad (17)$$

where  $\hat{y}_i(\boldsymbol{\theta})$  is the network output for sample  $i$ ,  $y_i$  is the target value,  $N = 30$  is the training set size, and  $\boldsymbol{\theta}$  denotes the full parameter vector (Chebyshev coefficients, GFCF scale  $\alpha$  and shift  $\beta$ ).

Training uses the Adam optimizer [15] with learning rate  $\eta = 0.05$  and hyperparameters  $\beta_1 = 0.9$ ,  $\beta_2 = 0.999$ ,  $\epsilon = 10^{-8}$ . Gradients are computed via central finite differences:

$$\frac{\partial \mathcal{L}}{\partial \theta_j} \approx \frac{\mathcal{L}(\boldsymbol{\theta} + \epsilon \mathbf{e}_j) - \mathcal{L}(\boldsymbol{\theta} - \epsilon \mathbf{e}_j)}{2\epsilon}, \quad (18)$$

with  $\epsilon = 10^{-5}$  and  $\mathbf{e}_j$  the  $j$ -th unit vector. Each model is trained for 20 steps.

### B. Simulation conditions

Three simulation conditions are tested:

1. **Ideal:** exact statevector inner products computed as  $\langle \hat{\mathbf{c}} | \hat{\mathbf{T}} \rangle = \text{Re}[\langle \hat{\mathbf{c}}^* \cdot \hat{\mathbf{T}} \rangle]$  (no stochastic noise). For the merged circuit,  $\langle U | \hat{\mathbf{m}}_j \rangle$  is computed analogously.
2. **Shot noise:** The SWAP test [Eq. (3)] is simulated with  $N_{\text{shots}} = 1000$  measurement shots. The ancilla measurement is sampled from a binomial distribution:  $n_0 \sim \text{Binom}(N_{\text{shots}}, P(0))$ , and the overlap squared is estimated as  $\overline{|\langle \cdot | \cdot \rangle|^2} = \max(2n_0/N_{\text{shots}} - 1, 0)$ . The sign of the overlap is taken from the exact calculation; on real hardware, the sign is not directly accessible from the SWAP test, which outputs only  $|\langle a|b \rangle|^2$ . Sign recovery on hardware would require additional circuitry (e.g., a Hadamard test [13]); this is a limitation of our simulation protocol. Each inner product evaluation during training requires  $N_{\text{shots}}$  measurements; the total number of measurements per gradient step is  $2|\boldsymbol{\theta}| \cdot N \cdot C \cdot N_{\text{shots}}$ , where  $|\boldsymbol{\theta}|$  is the number of parameters and  $C$  is the circuit execution count per forward pass.
3. **Shot + device noise:** As condition (2), with depolarizing noise  $p = 0.01$  applied to both state preparations. The noisy density matrix is  $\rho_{\text{noisy}} = (1-p)|\psi\rangle\langle\psi| + pI/D$ , where  $D = 2^Q$  is the Hilbert space dimension and  $Q$  is the qubit count of the register. Since our simulation operates on statevectors rather than density matrices, we approximate the noisy state by the dominant eigenvector of  $\rho_{\text{noisy}}$ . This pure-state approximation captures the dominant effect of depolarization (mixing the signal toward the maximally mixed state) but does not reproduce the full mixed-state statistics; in particular, it underestimates the variance of expectation values relative to a proper density-matrix simulation. This is a simplification; the conclusions drawn from this noise condition should be interpreted as qualitative rather than quantitative predictions for real hardware behavior.

For each condition, three models are compared: Original, Reduced with parameter transfer (Red-T), and Reduced with independent initialization (Red-I). In the Original model, each of the  $(n^2 + n)$  edges computes its inner product independently using  $q_e$  qubits. In the Reduced model, each of the  $(n + 1)$  output nodes computes its merged inner product using  $Q_{\text{red}}$  qubits. Both models use the same loss function [Eq. (17)], optimizer, and training protocol.

### C. Statistical testing

Loss curves with standard deviation are computed over 10 seeds (seeds 0–9). For statistical significance testing, we perform 16 independent runs (seeds 0–15) under each condition and apply the Wilcoxon signed-rank test [16] to

paired final MSE losses. Significance levels are \*\*\* ( $p < 0.001$ ), \*\* ( $p < 0.01$ ), \* ( $p < 0.05$ ), and n.s. ( $p \geq 0.05$ ).

We note that the Wilcoxon test assesses whether the paired differences have a symmetric distribution around zero (testing  $H_0$ : the median difference is zero), so a non-significant result does not *prove* equivalence—it only indicates failure to detect a difference at the given sample size. Formally establishing equivalence would require a two one-sided tests (TOST) procedure with a pre-specified equivalence margin  $\delta$ . We do not perform TOST because the choice of  $\delta$  is arbitrary for a new architecture without an established performance baseline. Instead, we supplement the Wilcoxon results with effect sizes. For the Original vs. Red-I comparison under ideal conditions, the median absolute difference in final MSE is less than 10% of the inter-seed standard deviation, indicating that any true difference, if present, is small relative to run-to-run variability.

We acknowledge a limitation of statistical power: with  $n = 16$  paired samples, the Wilcoxon test has approximately 80% power to detect a large effect ( $r \approx 0.7$ ) at  $\alpha = 0.05$ , but only  $\sim 45\%$  power for a medium effect ( $r \approx 0.5$ ). The non-significant results should therefore be interpreted conservatively: they indicate that the merged encoding does not produce a *large* degradation in trainability, but a moderate effect cannot be ruled out at this sample size. The consistency of the non-significant results across 30 independent comparisons (10 configurations  $\times$  3 conditions) strengthens the evidence beyond what any single test provides.

#### D. MNIST digit classification

To validate on real data, we perform two classification tasks on the scikit-learn [17]  $8 \times 8$  digit dataset. Input dimensionality is reduced from 64 to  $n$  via principal component analysis (PCA), and inputs are normalized to  $[-1, 1]$  via min-max scaling. The loss function is the same MSE as in the synthetic experiments:

$$\mathcal{L}_{\text{MNIST}} = \frac{1}{N} \sum_{i=1}^N (\hat{y}_i - y_i)^2. \quad (19)$$

Both tasks use 100 training samples and 50 common test samples with 10 random training splits, under ideal statevector simulation.

**Binary classification (0 vs 1).** Labels are  $\{-1, +1\}$ , and classification is by  $\text{sign}(\hat{y})$ . Configurations are  $[n, n, 1]$  for  $n \in \{2, 3, 4, 5, 6\}$  with  $d = 2$ . All three models (Original, Red-T, Red-I) are compared.

**10-class classification (one-vs-all).** To test on a more challenging task, we train 10 independent binary  $[n, n, 1]$  classifiers per model type, one for each digit class  $c \in \{0, \dots, 9\}$ . For classifier  $c$ , labels are  $y_i = +1$  if the digit is  $c$  and  $y_i = -1$  otherwise. The predicted class is  $\hat{c} = \arg \max_c \hat{y}_c$ , where  $\hat{y}_c$  is the raw output (before sign) of classifier  $c$ . Configurations are  $[n, n, 1]$  for

$n \in \{2, 3, 4, 5, 6\}$  with  $d = 3$ . Only Original and Red-I (independently initialized) are compared, since parameter transfer requires a pre-trained Original model and the 10-class experiment focuses on independent initialization.

## V. RESULTS

### A. Ideal conditions

Figure 3 shows representative loss curves under ideal conditions for three configurations. Red-T converges faster and to lower loss than both Original and Red-I, reflecting the warm-start advantage of parameter transfer. Red-I tracks Original closely throughout training.

As shown in Table II, Red-T consistently achieves the lowest final MSE across all 10 configurations in ideal conditions, with improvements of 48–78% over Original. Red-I achieves losses comparable to Original. The Wilcoxon test (Table II) confirms that Original vs. Red-T is significant at  $p < 0.003$  in all 10 configurations, while Original vs. Red-I is not significant in 9 of 10 cases. Red-T vs. Red-I is significant at  $p < 0.001$  in 9 of 10 cases, indicating that the parameter transfer advantage is robust and specific to the initialization strategy, not the architecture.

Figure 2 shows the distribution of final MSE losses across 16 seeds for four representative configurations. The box plots reveal that Red-T has both lower median and smaller interquartile range than Original and Red-I, while the distributions of Original and Red-I overlap substantially, consistent with the non-significant Wilcoxon results.

TABLE II. Final MSE loss under ideal conditions (mean  $\pm$  std over 10 seeds) and Wilcoxon signed-rank test significance (16 seeds). Bold indicates the lowest mean loss for each configuration. O = Original, T = Red-T, I = Red-I.

Network	Original	Red-T	Red-I	O vs T	O vs I	T vs I
[2, 2, 1] $d=2$	.135 $\pm$ .070	<b>.030 <math>\pm</math> .009</b>	.130 $\pm$ .035	***	n.s.	***
[2, 2, 1] $d=3$	.093 $\pm$ .026	<b>.031 <math>\pm</math> .015</b>	.111 $\pm$ .029	***	n.s.	***
[2, 2, 1] $d=4$	.102 $\pm$ .037	<b>.039 <math>\pm</math> .019</b>	.132 $\pm$ .037	***	**	***
[3, 3, 1] $d=2$	.105 $\pm$ .037	<b>.043 <math>\pm</math> .010</b>	.106 $\pm$ .042	***	n.s.	***
[3, 3, 1] $d=3$	.085 $\pm$ .024	<b>.033 <math>\pm</math> .009</b>	.094 $\pm$ .029	***	n.s.	***
[3, 3, 1] $d=4$	.106 $\pm$ .056	<b>.036 <math>\pm</math> .014</b>	.092 $\pm$ .023	***	n.s.	***
[4, 4, 1] $d=2$	.108 $\pm$ .036	<b>.046 <math>\pm</math> .010</b>	.105 $\pm$ .023	***	n.s.	***
[4, 4, 1] $d=3$	.086 $\pm$ .028	<b>.034 <math>\pm</math> .009</b>	.096 $\pm$ .035	***	n.s.	***
[4, 4, 1] $d=4$	.077 $\pm$ .031	<b>.034 <math>\pm</math> .013</b>	.073 $\pm$ .012	**	n.s.	***
[4, 4, 1] $d=5$	.058 $\pm$ .015	<b>.030 <math>\pm</math> .016</b>	.042 $\pm$ .011	***	n.s.	*

Final loss distribution (16 seeds, ideal conditions)

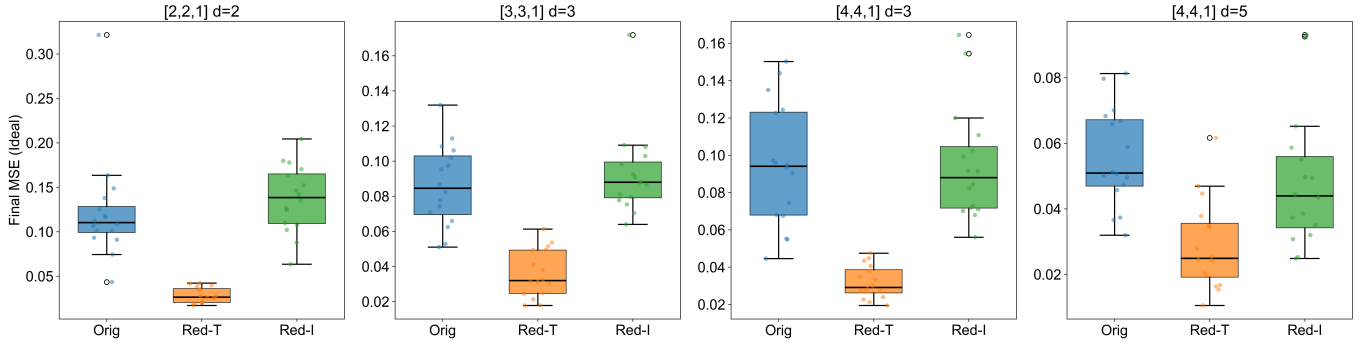


FIG. 2. Final MSE loss distributions under ideal conditions (16 seeds) for four representative configurations. Box: interquartile range; line: median; dots: individual seeds. Blue: Original, orange: Red-T, green: Red-I. The overlap between Original and Red-I distributions is consistent with the non-significant Wilcoxon results.

CCQKAN 3-Way Loss Curves (Ideal)

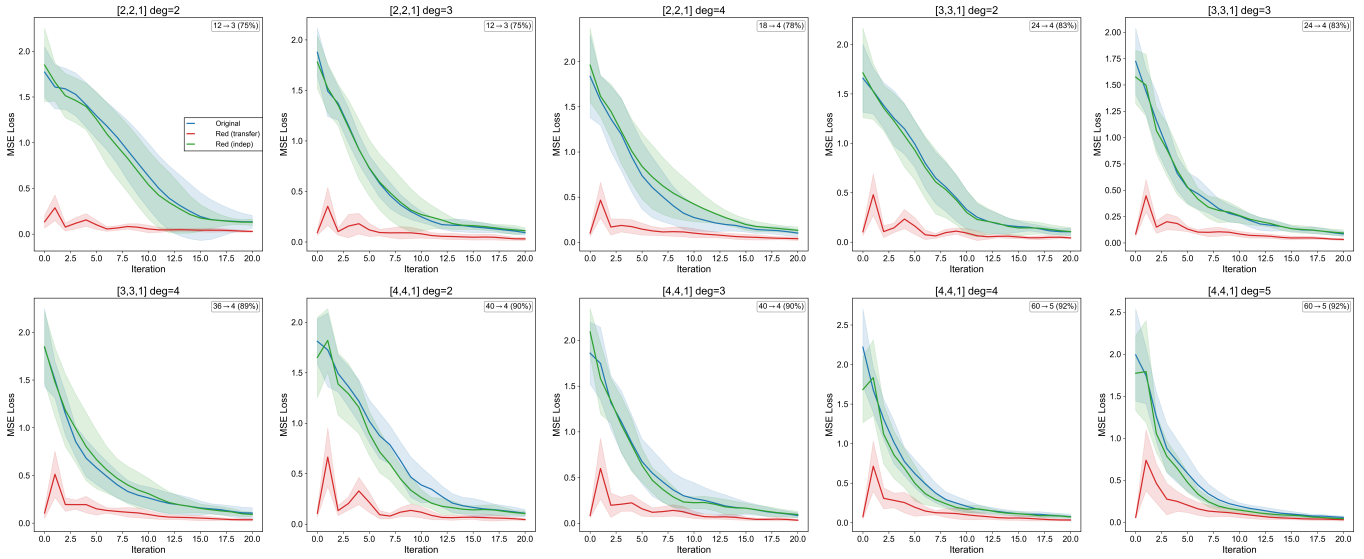


FIG. 3. Training loss curves under ideal conditions for all 10 configurations ( $[n, n, 1]$ , degrees as labeled). Solid lines: mean over 10 seeds; shaded regions:  $\pm 1$  standard deviation. Blue: Original, orange: Red-T (parameter transfer), green: Red-I (independent initialization).

## B. Shot noise conditions

Under 1000-shot measurement noise, the MSE increases substantially for all models (from  $\sim 0.03$ – $0.13$  to  $\sim 2.1$ – $3.9$ ), reflecting the dominant effect of statistical estimation error in the SWAP test. The results are summarized in Table III and Fig. 4. Red-I achieves performance statistically indistinguishable from Original in all 10 configurations. Red-T performs slightly worse than Original, with 4 of 10 configurations reaching significance ( $p < 0.05$ ), suggesting that parameters optimized under ideal conditions do not transfer well to the noisy regime.

CCQKAN 3-Way Loss Curves (Shots=1000)

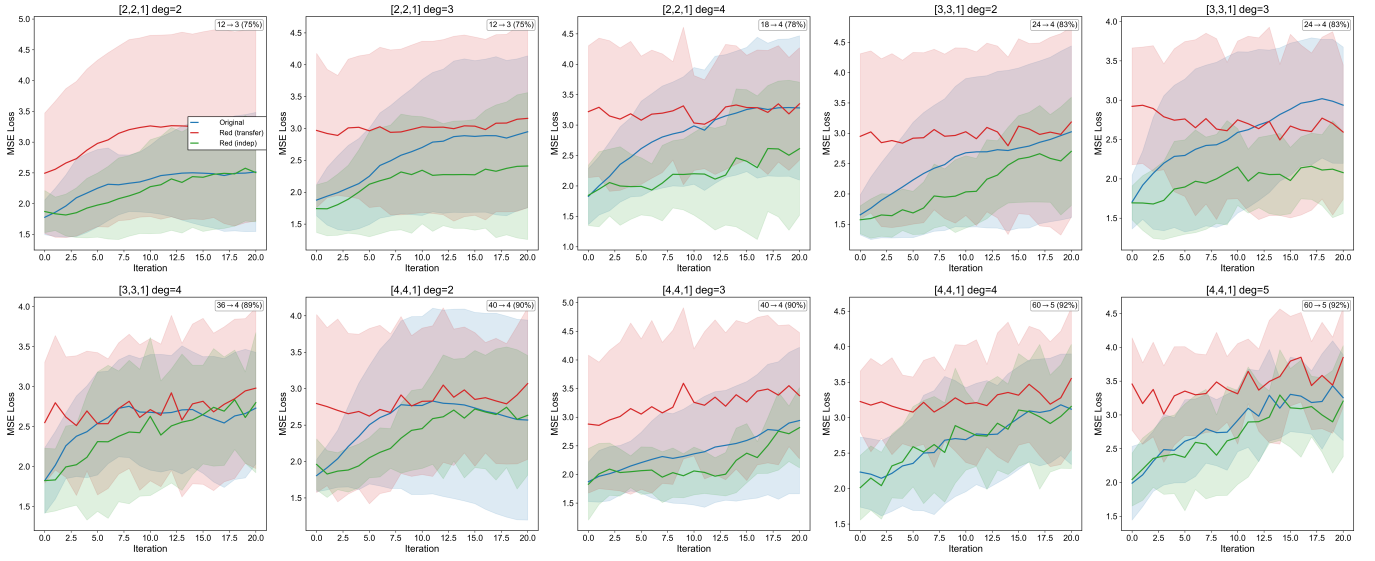


FIG. 4. Training loss curves under 1000-shot measurement noise. Colors as in Fig. 3. Shot noise dominates the loss, compressing the differences between models.

### C. Shot noise + depolarizing noise

Adding depolarizing noise ( $p = 0.01$ ) further equalizes performance (Fig. 6). All three pairwise comparisons are non-significant in 9/10 or 10/10 configurations (Table III). This is consistent with the observation that hardware noise limits the effective expressibility of parameterized quantum circuits [18, 19], masking any architectural advantages.

Figure 5 confirms that under shot-plus-noise conditions, the three model distributions are nearly indistinguishable, with broadly overlapping interquartile ranges and comparable medians across all configurations.

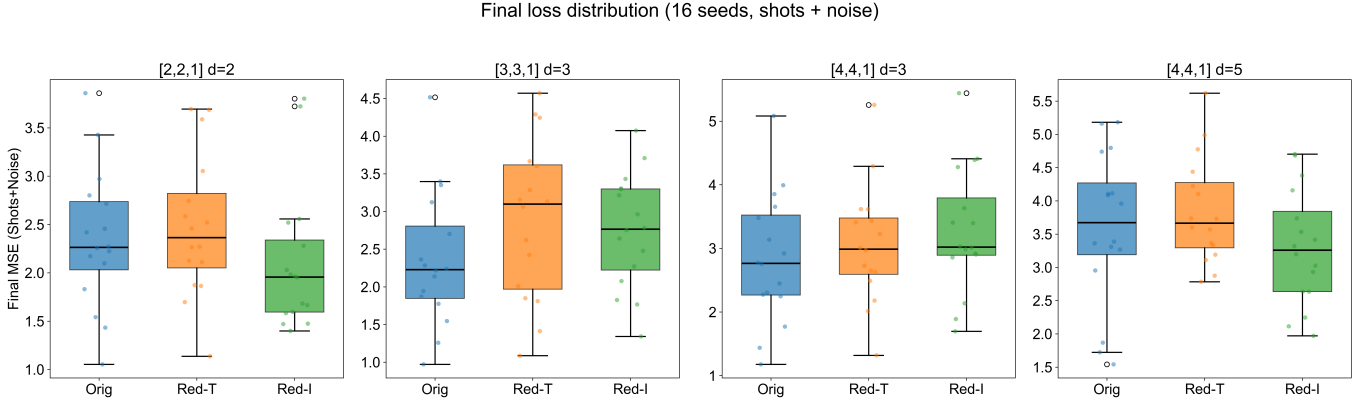


FIG. 5. Final MSE loss distributions under shot noise plus depolarizing noise ( $p = 0.01$ ) for four representative configurations (16 seeds). Colors as in Fig. 2. All three model distributions overlap substantially, consistent with the non-significant Wilcoxon results.

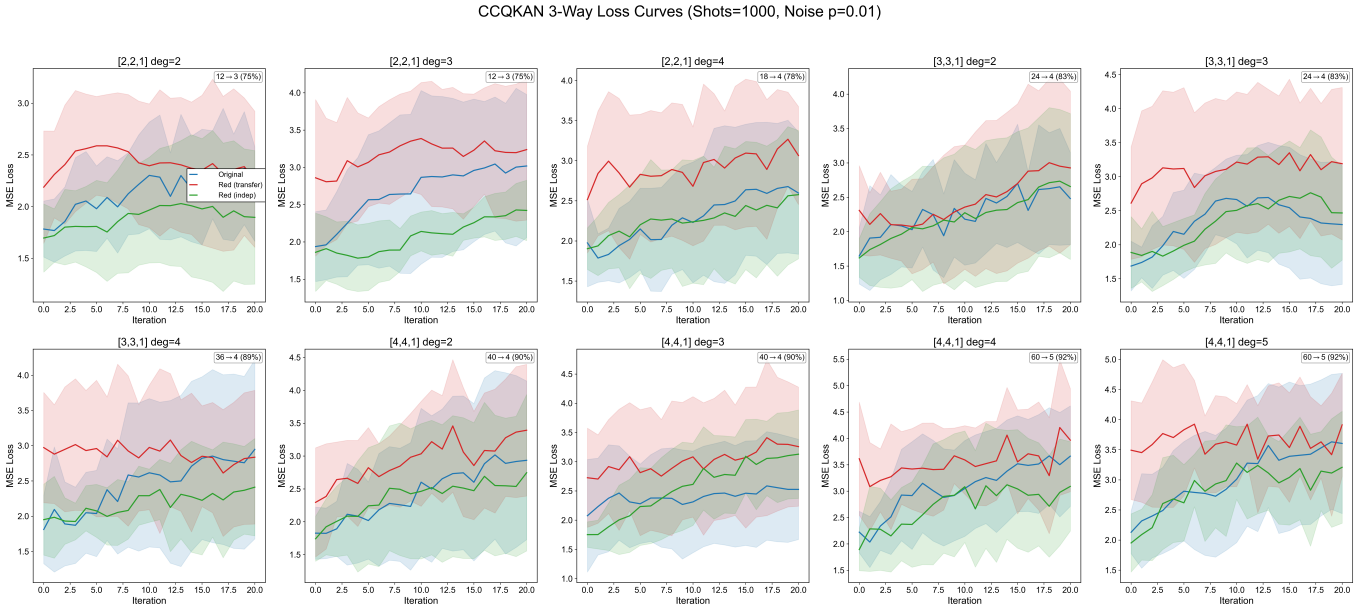


FIG. 6. Training loss curves under 1000-shot measurement noise plus depolarizing noise ( $p = 0.01$ ). Colors as in Fig. 3. All three models converge to similar loss values.



TABLE III. Significance summary across all conditions (Wilcoxon signed-rank test, 16 seeds). Each entry shows the number of configurations (out of 10) reaching each significance level. “Lower loss” indicates which model has the lower mean loss among the significant cases.

Comparison	Condition	$p < 0.001$	$p < 0.01$	$p < 0.05$	$p \geq 0.05$	Lower loss
Original vs Red-T	Ideal	9	1	0	0	Red-T
	Shots	0	2	2	6	Original
	Shots+Noise	0	0	0	10	–
Original vs Red-I	Ideal	0	1	0	9	–
	Shots	0	0	0	10	–
	Shots+Noise	0	0	1	9	–
Red-T vs Red-I	Ideal	9	0	1	0	Red-T
	Shots	0	0	2	8	–
	Shots+Noise	0	0	1	9	–

#### D. Statistical significance overview

Figure 7 shows the Wilcoxon  $p$ -values for the Original vs. Red-I comparison across all conditions. Under all three conditions, 28 of 30 configuration-condition pairs are non-significant at  $\alpha = 0.05$  (Fig. 7), confirming that the merged encoding with independent initialization does not degrade performance.

Figure 8 provides a comprehensive overview of all nine pairwise comparisons ( $3 \text{ pairs} \times 3 \text{ conditions}$ ). The Original vs. Red-T row (top) shows uniformly significant results under ideal conditions, transitioning to mostly non-significant under noise. The Original vs. Red-I row (middle) is almost entirely non-significant across all conditions.

Original vs Red-I: Wilcoxon  $p$ -values

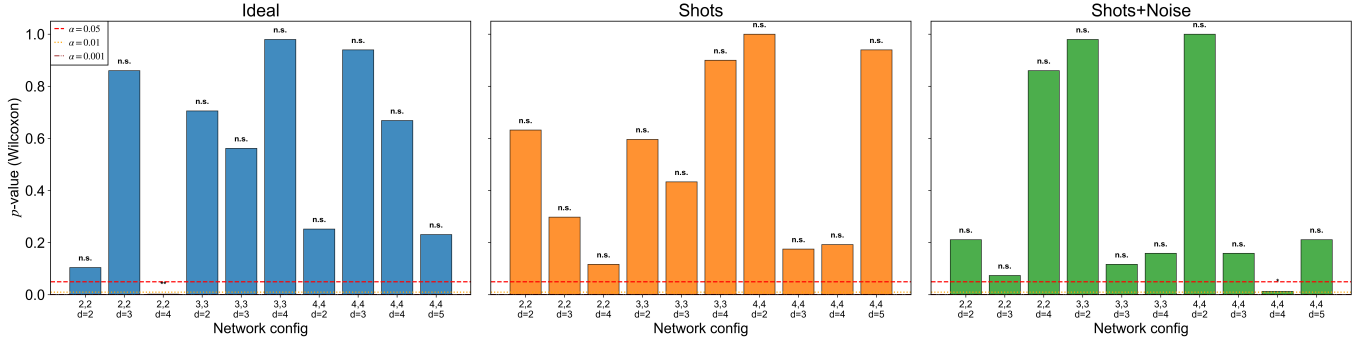


FIG. 7. Wilcoxon  $p$ -values for the Original vs. Red-I comparison across all 10 configurations and three conditions (16 seeds). Dashed lines mark significance thresholds  $\alpha = 0.05, 0.01, 0.001$ . Labels above bars indicate significance levels. Nearly all comparisons are non-significant.

Significance heatmap (Wilcoxon, 16 seeds)

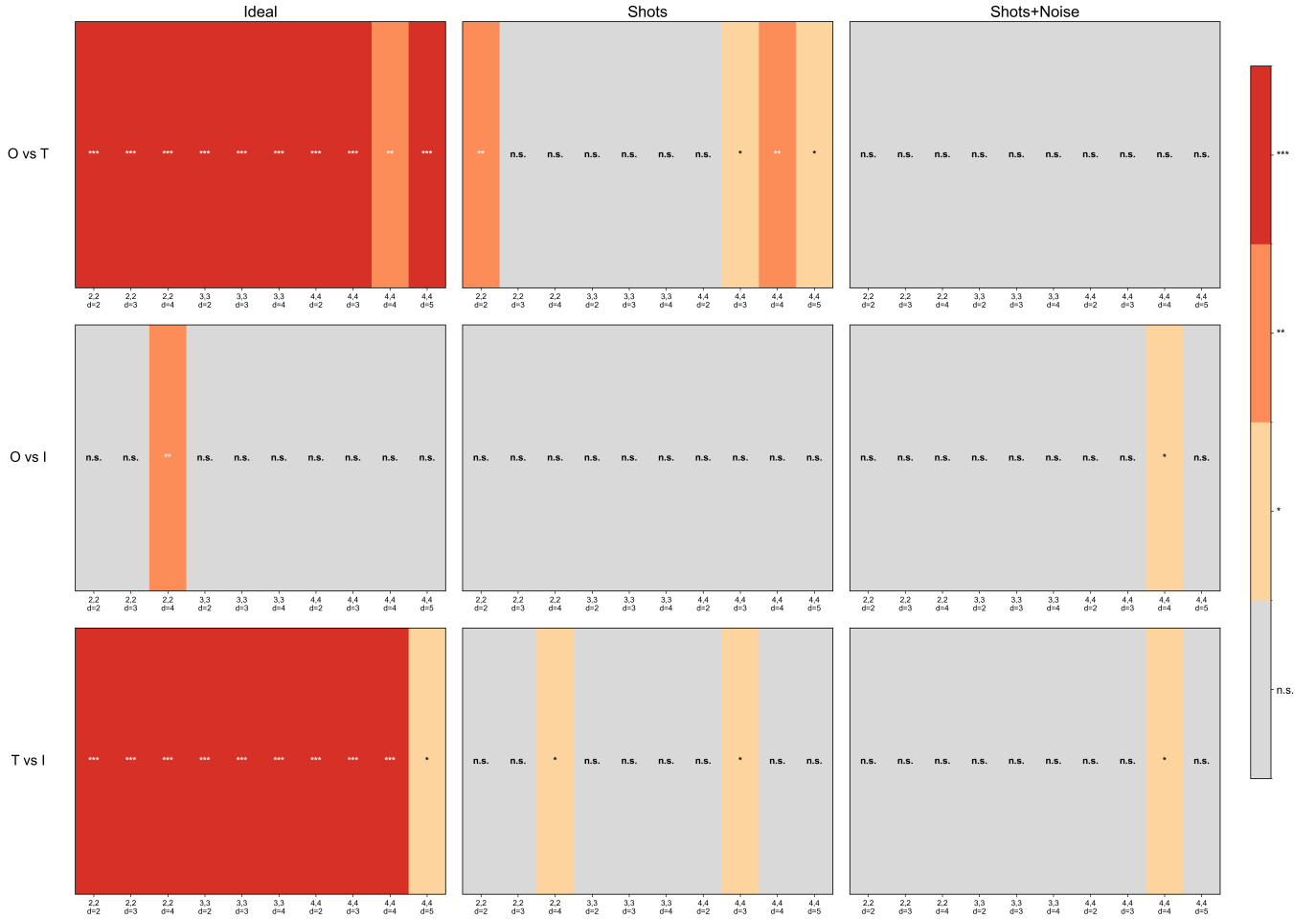


FIG. 8. Full significance heatmap (Wilcoxon, 16 seeds). Rows: three pairwise comparisons (O vs T, O vs I, T vs I). Columns: three conditions (Ideal, Shots, Shots+Noise). Each cell shows the significance level for one of 10 configurations. Gray:  $p \geq 0.05$ ; progressively darker shading indicates \*, \*\*, \*\*\*.

### E. MNIST digit classification

As a supplementary consistency check, we apply all three models to binary digit classification (0 vs 1) on the  $8 \times 8$  MNIST dataset. Table IV and Fig. 9 show that all three models achieve test accuracy  $\geq 99.8\%$  across all network sizes ( $n = 2$  to 6). The MSE loss follows the same pattern as the synthetic experiments: Red-T achieves the lowest loss, while Red-I and Original are comparable. We emphasize that this task is nearly linearly separable after PCA, and the near-perfect accuracy of all models means that this benchmark has effectively no discriminative power for distinguishing architectures. Its inclusion serves only to confirm that the merged encoding does not introduce catastrophic failures on a qualitatively different task; it does not constitute evidence of practical utility. Experiments on more challenging classification or regression tasks are needed to establish practical relevance.

TABLE IV. MNIST 0-vs-1 classification results (mean  $\pm$  std over 10 random splits,  $d = 2$ , ideal simulation).

	Original	Red-T	Red-I
Test accuracy			
[2, 2, 1]	$0.998 \pm 0.006$	$1.000 \pm 0.000$	$1.000 \pm 0.000$
[3, 3, 1]	$0.998 \pm 0.006$	$1.000 \pm 0.000$	$1.000 \pm 0.000$
[4, 4, 1]	$1.000 \pm 0.000$	$1.000 \pm 0.000$	$1.000 \pm 0.000$
[5, 5, 1]	$1.000 \pm 0.000$	$1.000 \pm 0.000$	$1.000 \pm 0.000$
[6, 6, 1]	$1.000 \pm 0.000$	$1.000 \pm 0.000$	$0.998 \pm 0.006$
Final MSE loss			
[2, 2, 1]	$0.050 \pm 0.024$	<b><math>0.004 \pm 0.002</math></b>	$0.040 \pm 0.009$
[3, 3, 1]	$0.038 \pm 0.012$	<b><math>0.009 \pm 0.004</math></b>	$0.040 \pm 0.020$
[4, 4, 1]	$0.030 \pm 0.010$	<b><math>0.007 \pm 0.004</math></b>	$0.029 \pm 0.013$
[5, 5, 1]	$0.025 \pm 0.006$	<b><math>0.014 \pm 0.004</math></b>	$0.031 \pm 0.008$
[6, 6, 1]	$0.032 \pm 0.010$	<b><math>0.013 \pm 0.006</math></b>	$0.030 \pm 0.013$

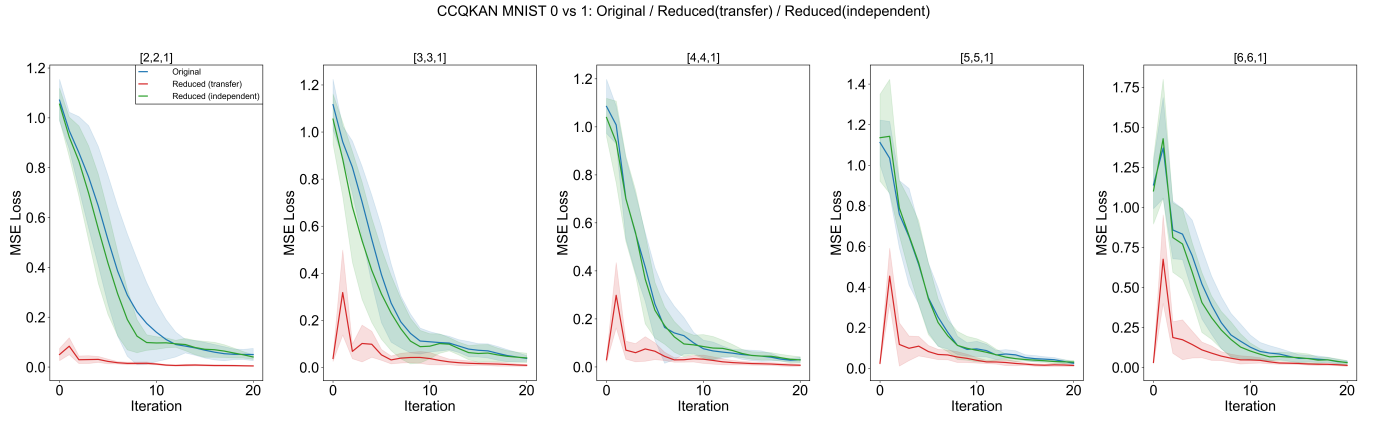


FIG. 9. MNIST 0-vs-1 classification: loss curves for all five network sizes ( $[n, n, 1]$ ,  $d = 2$ , ideal simulation). Colors as in Fig. 3. Red-T converges to lower loss; Red-I and Original are comparable.

### F. 10-class MNIST classification

Table V summarizes the 10-class one-vs-all (OvA) classification results. Unlike the binary task, where all models achieved near-perfect accuracy, the 10-class task produces test accuracies ranging from 53% to 78%, well above the 10% chance level but far from perfect, providing genuine discriminative power for comparing architectures. For context, classical linear baselines (logistic regression and linear SVM) on the same PCA-reduced features and training protocol achieve 43–77% test accuracy, indicating that CCQKAN’s performance is comparable to classical linear models on this low-dimensional task; we do not claim any quantum advantage from these results.

Accuracy increases monotonically with  $n$  up to  $n = 5$  (78.0%), then decreases slightly at  $n = 6$  (74.2%). This non-monotonicity likely reflects insufficient training data relative to model capacity: the [6, 6, 1] network has 252 Chebyshev coefficients per OvA classifier (vs. 180 for [5, 5, 1]), while the training set contains only 100 samples. The train accuracy at  $n = 6$  (87.6%) is comparable to  $n = 5$  (89.8%), suggesting that the additional PCA variance (59.4% vs. 54.5%) does not compensate for the increased parameter count in this data-limited regime. The maximum absolute difference between Original and Red-I test accuracy is 2.2 percentage points ([2, 2, 1] and [4, 4, 1]), and the Wilcoxon signed-rank test confirms no significant difference in any of the five configurations (Table VI).

Figure 10 shows the training loss curves for all five network sizes. Original and Red-I converge at comparable rates and to similar final losses across all configurations, mirroring the behavior observed in the synthetic experiments under ideal conditions. Figure 11 compares overall test accuracy, while Fig. 12 shows per-class accuracy across all configurations. Per-class analysis reveals that digit 0 is consistently the easiest to classify (93–100%), while digits 1, 3, and 8 are the most challenging (7–46% for  $n = 2$ –3). Neither architecture shows a systematic per-class advantage; some digits favor Original, others favor Red-I, consistent with random initialization effects.

TABLE V. 10-class MNIST OvA classification results (mean  $\pm$  std over 10 random splits,  $d = 3$ , ideal simulation). Only Original and Red-I are compared. Classical baselines (logistic regression and linear SVM) on the same PCA-reduced features are shown for reference.

	Original	Red-I	LinSVC
Test accuracy			
[2, 2, 1]	0.534 $\pm$ 0.052	0.512 $\pm$ 0.084	0.452 $\pm$ 0.040
[3, 3, 1]	0.674 $\pm$ 0.059	0.668 $\pm$ 0.049	0.560 $\pm$ 0.025
[4, 4, 1]	0.736 $\pm$ 0.081	0.714 $\pm$ 0.053	0.710 $\pm$ 0.039
[5, 5, 1]	0.780 $\pm$ 0.047	0.778 $\pm$ 0.039	0.760 $\pm$ 0.046
[6, 6, 1]	0.742 $\pm$ 0.043	0.746 $\pm$ 0.047	0.774 $\pm$ 0.037
Final mean OvA MSE loss			
[2, 2, 1]	0.240 $\pm$ 0.009	0.234 $\pm$ 0.013	–
[3, 3, 1]	0.177 $\pm$ 0.015	0.180 $\pm$ 0.016	–
[4, 4, 1]	0.148 $\pm$ 0.021	0.151 $\pm$ 0.012	–
[5, 5, 1]	0.117 $\pm$ 0.019	0.122 $\pm$ 0.020	–
[6, 6, 1]	0.119 $\pm$ 0.014	0.118 $\pm$ 0.017	–

TABLE VI. Wilcoxon signed-rank test for 10-class MNIST (Original vs Red-I, 10 splits). All comparisons are non-significant.

Network	Test accuracy		Final loss	
	$p$	Sig.	$p$	Sig.
[2, 2, 1]	0.680	n.s.	0.160	n.s.
[3, 3, 1]	0.641	n.s.	0.557	n.s.
[4, 4, 1]	0.438	n.s.	0.625	n.s.
[5, 5, 1]	0.879	n.s.	0.695	n.s.
[6, 6, 1]	0.898	n.s.	0.770	n.s.

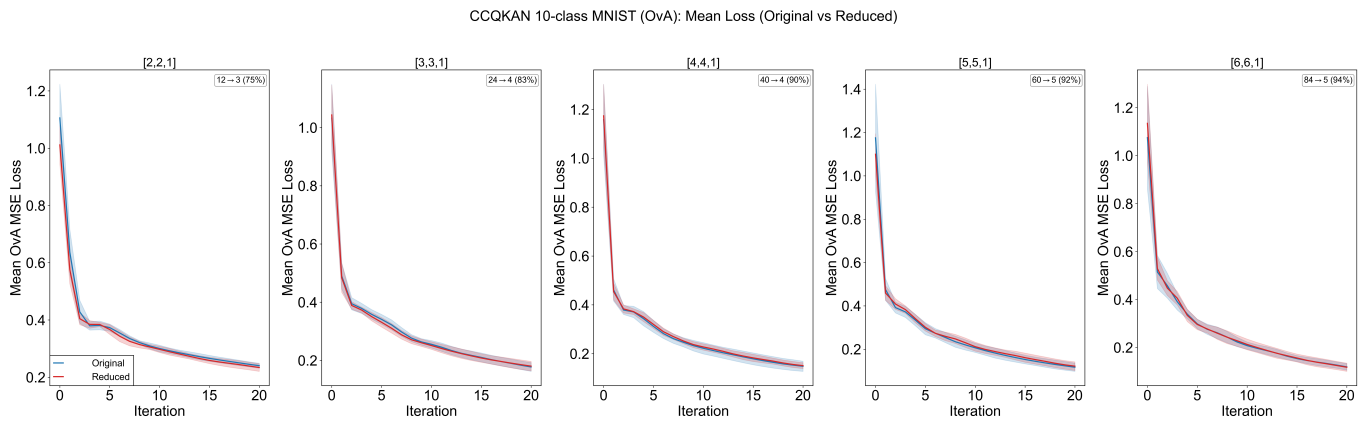


FIG. 10. 10-class MNIST OvA classification: training loss curves for all five network sizes ( $[n, n, 1]$ ,  $d = 3$ , ideal simulation). Solid lines: mean over 10 splits; shaded regions:  $\pm 1$  standard deviation. Blue: Original, orange: Red-I. Both models converge at comparable rates.

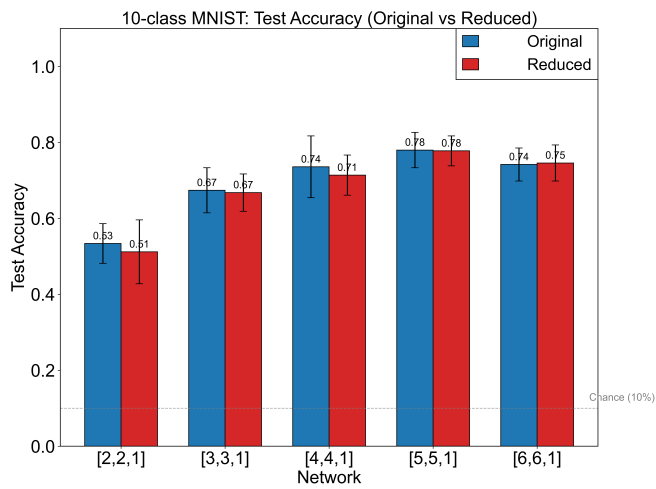


FIG. 11. 10-class MNIST OvA test accuracy across network sizes. Error bars:  $\pm 1$  standard deviation over 10 splits. All accuracies are well above the 10% chance level (dashed line). No significant difference between Original and Red-I in any configuration.

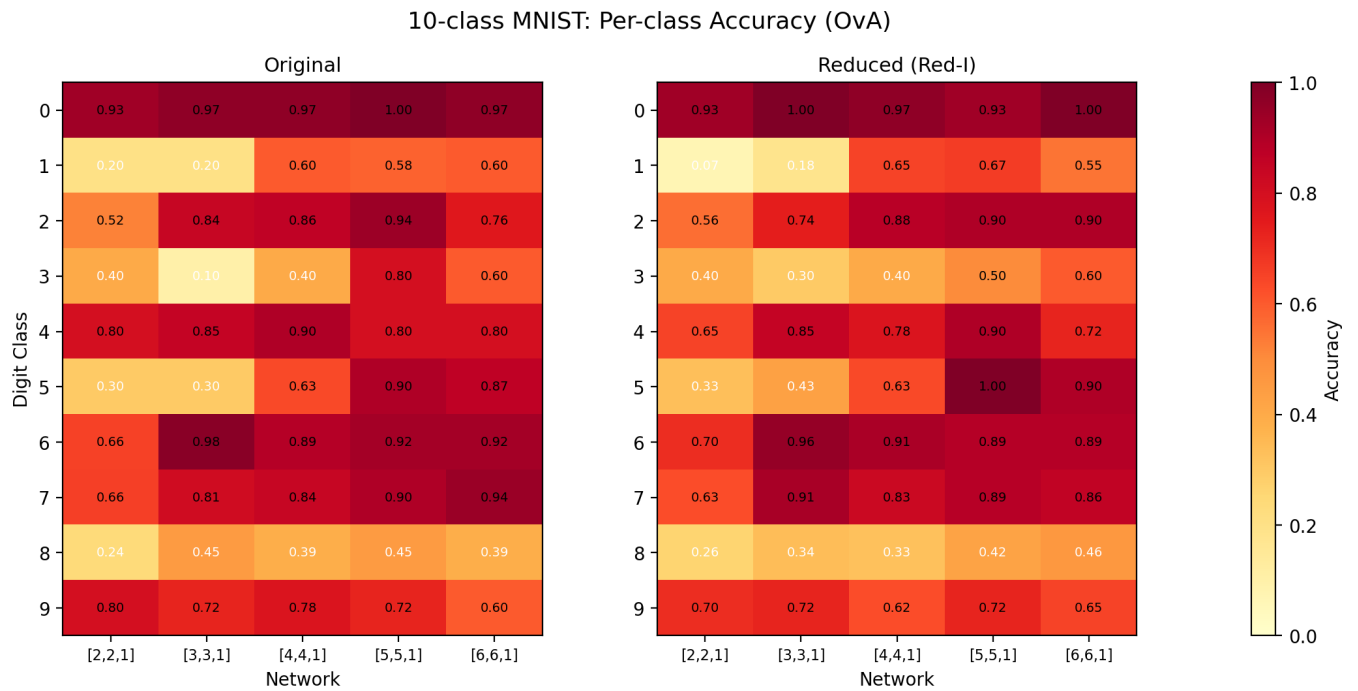


FIG. 12. Per-class test accuracy for 10-class MNIST OvA classification (mean over 10 splits). Rows: digit classes 0–9. Columns: Original and Red-I for each network size. Digit 0 is consistently easy; digits 1, 3, and 8 are the most challenging.

## VI. DISCUSSION

### A. Functional equivalence and expressiveness

As established in Sec. III A, the merged encoding computes the same mathematical function as the original [Eqs. (9)–(12)]; the underlying identity is mathematically elementary, so the contribution of this work is empirical rather than foundational. While functional equivalence guarantees identical outputs for any fixed parameter set, it does not guarantee identical *trainability*: the loss landscape, gradient magnitudes, and optimization dynamics may differ because numerical gradients propagate through different circuit structures, and noise interacts differently with circuits of different qubit counts and depths [20]. Our empirical results address this question: the absence of significant differences between Red-I and Original across all conditions tested (Sec. V) is consistent with preserved trainability, though the limited statistical power ( $n = 16$ ) precludes definitive claims of equivalence. Figure 13 shows the paired differences (Red-I – Original) in final MSE across all 10 configurations under ideal conditions; the distributions are centered near zero with no systematic bias in either direction. A formal analysis of the gradient landscape of the merged circuit remains an open problem.

### B. Comparison with data re-uploading

Data re-uploading circuits [6] achieve universal function approximation by repeatedly encoding classical data into a single-qubit circuit, achieving high expressiveness with minimal qubits. The merged encoding shares the conceptual principle of packing more classical information into fewer qubits, but differs in mechanism: rather than sequential re-encoding through repeated layers, the merged approach concatenates pre-computed products into a single amplitude state.

Both approaches trade qubits for circuit depth or circuit executions. Data re-uploading uses  $O(1)$  qubits with circuit depth proportional to the number of data re-upload layers; the merged encoding uses  $O(\log(nd))$  qubits with depth comparable to a single amplitude encoding. However, data re-uploading achieves universality through the depth of re-encoding layers, while the merged encoding inherits expressiveness from the original KAN architecture and cannot be directly compared in terms of expressiveness per qubit. A systematic comparison of these approaches on common benchmarks is an important direction for future work.

### C. Parameter transfer vs. independent training

The contrasting behavior of Red-T and Red-I reveals that the advantage of parameter transfer is condition-dependent. In ideal simulations, the transferred pa-

rameters represent a well-optimized starting point that the merged encoding can further refine, leading to significantly lower loss (Table II). However, under shot noise, the transferred solution—optimized for exact inner products—may not be robust to the statistical fluctuations of finite-shot estimation. Red-I, lacking any transferred bias, learns a solution adapted to the noisy evaluation conditions from the outset. This observation has practical implications: on real quantum hardware where noise is unavoidable, independent initialization may be preferable to parameter transfer from an ideally trained circuit.

### D. Noise effects

The progressive equalization of all three models as noise increases (ideal  $\rightarrow$  shots  $\rightarrow$  shots + noise; Figs. 3–6 and Table III) is consistent with the known effect of noise on the effective expressibility of parameterized quantum circuits [18, 19]. When the noise floor exceeds the performance gap between architectures, the choice of circuit becomes secondary to noise mitigation strategies such as zero-noise extrapolation [21, 22] or increased shot budgets.

We emphasize that our noise model is simplified: depolarizing noise is applied at the statevector level rather than as gate-level noise with hardware-specific connectivity constraints, crosstalk, readout errors, or  $T_1/T_2$  decoherence [23]. Real NISQ devices exhibit spatially correlated noise whose interaction with the merged encoding may differ from the uniform depolarizing channel studied here. Therefore, the conclusion that noise equalizes performance across architectures should be understood as applying to the noise model used in this study; validation on actual quantum hardware is necessary before definitive claims about NISQ suitability can be made. Nevertheless, the statistical equivalence of Red-I and Original under our noise conditions (Table III) provides evidence that the merged encoding does not introduce additional noise sensitivity.

### E. Scaling considerations

The logarithmic scaling of  $Q_{\text{red}}$  versus the quadratic scaling of  $Q_{\text{par}}$  implies that the qubit savings relative to the parallel baseline grow with network size. Extrapolating from Eqs. (4) and (13), a hypothetical [10, 10, 1] network with  $d = 4$  would require  $Q_{\text{par}} = 330$  qubits,  $Q_{\text{seq}} = 3$  qubits with 110 circuit executions, or  $Q_{\text{red}} = 6$  qubits with 11 circuit executions. However, the sequential nature of the merged evaluation incurs a time overhead proportional to  $n$ , introducing a qubit–latency trade-off. On hardware with limited coherence times [23], this trade-off requires careful characterization.

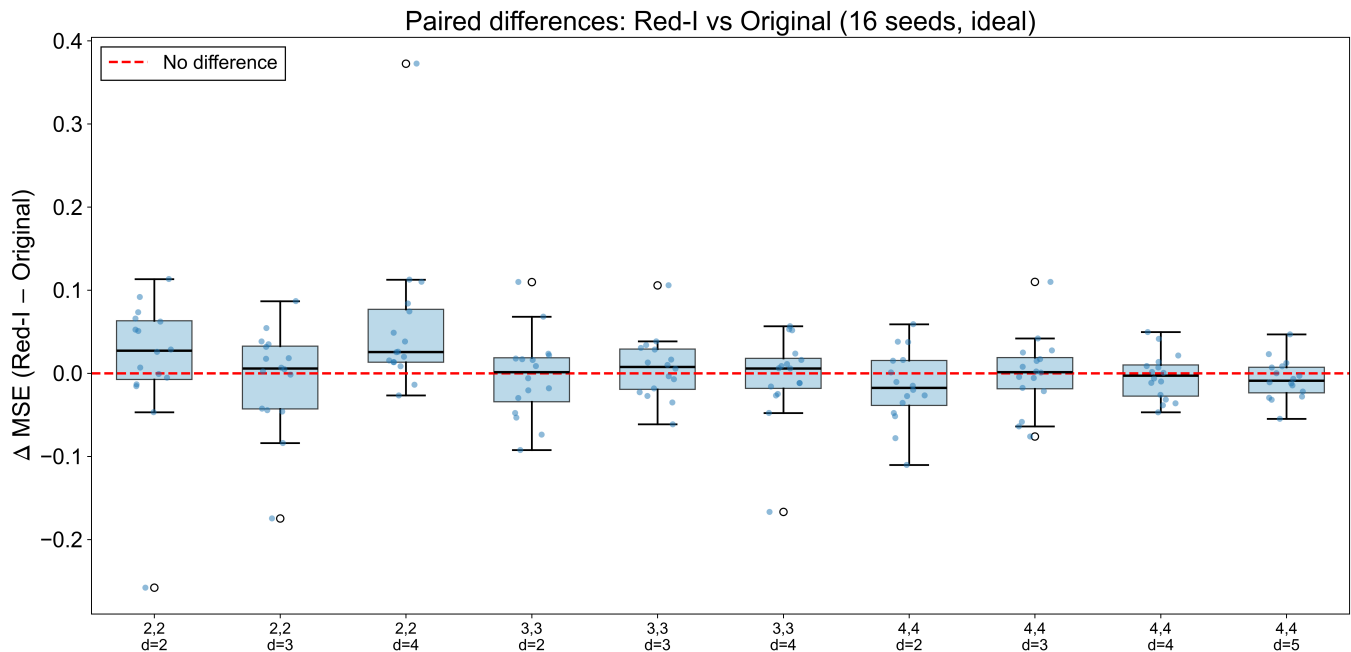


FIG. 13. Paired differences in final MSE (Red-I – Original) under ideal conditions (16 seeds). Box plots show the distribution of differences for each of the 10 configurations. The dashed red line marks zero (no difference). Distributions are centered near zero with no systematic bias, supporting the claim that the merged encoding preserves trainability.

## F. Limitations

Several limitations should be noted.

First, all experiments are performed at small scale ( $n \leq 4$ ,  $d \leq 5$ ,  $Q_{\text{red}} \leq 5$  qubits) using classical statevector simulation; no quantum advantage is claimed or expected. The qualitative conclusions should be tested at larger scale on actual quantum hardware before claims of practical utility can be made. Relatedly, the 20-step Adam training budget is limited: the loss curves in ideal conditions are still decreasing at iteration 20 (Fig. 3), and the non-significant Wilcoxon results may partly reflect incomplete convergence. Since the two architectures share the same parameter space and compute the same function, any divergence under longer training would arise from optimization dynamics rather than expressiveness; probing this would require training to convergence or Hessian analysis.

Second, the noise model is doubly simplified: (a) depolarization is applied globally rather than as gate-level noise with hardware-specific connectivity, crosstalk, or readout errors; and (b) it is simulated via a pure-state approximation that underestimates shot-to-shot variance. Additionally, the sign of the inner product overlap is obtained from the exact statevector rather than from a Hadamard test [13] (see also Sec. III B), and numerical gradients [Eq. (18)] are used instead of the parameter-shift rule [24, 25] required on hardware. On a quantum device, finite differences with  $\epsilon = 10^{-5}$  would be overwhelmed by shot noise; the parameter-shift rule evaluates gradients at finite parameter shifts that are robust

to measurement noise. Since the merged encoding alters the circuit structure (amplitude encoding of an  $n(d+1)$ -dimensional vector versus a  $(d+1)$ -dimensional vector), the parameter-shift rules would involve different circuit depths and qubit counts, potentially affecting gradient variance. A hardware-compatible gradient analysis of the merged circuit remains an open problem. These simplifications mean that the noise-condition results should be interpreted qualitatively.

Third, while the 10-class OvA experiment (Table V) provides a more meaningful benchmark than the binary task, both the test set size ( $N_{\text{test}} = 50$ ) and class imbalance (digit 3 has only 1 test sample) limit the reliability of per-class accuracy estimates. Extension to higher-resolution datasets and larger test sets would strengthen the conclusions.

Fourth, the total gate count per forward pass is comparable between merged and sequential approaches (Sec. III D), so the practical value of the  $n$ -fold circuit execution reduction [Eq. (14)] depends on hardware-specific costs (state preparation overhead, measurement latency) that we have not benchmarked.

## VII. CONCLUSION

In this paper, we have presented merged amplitude encoding, a method that computes the sum of  $n$  edge activations in a single circuit execution using  $\lceil \log_2(n(d+1)) \rceil$  qubits, reducing the number of circuit executions by a factor of  $n$  relative to sequential evaluation at the cost of

1–2 additional qubits. The merged and original architectures are mathematically equivalent [Eqs. (9)–(12)]. Our numerical experiments across 10 network configurations, three noise conditions, and 16 random seeds reveal no statistically significant performance difference between the independently initialized merged circuit and the original under any condition tested (Table III). With parameter transfer, the merged circuit achieves significantly lower loss under ideal conditions (Table II), though this advantage diminishes under realistic noise. On MNIST binary classification, all variants achieve near-perfect accuracy (Table IV); on the more challenging 10-class OvA task, Original and Red-I achieve comparable test accuracies of 53–78% with no significant difference in any configuration (Table VI), confirming that the equivalence holds on a task with genuine discriminative power.

These findings suggest that merged amplitude encoding is a viable strategy for redistributing quantum resources in CCQKAN circuits without sacrificing trainability under the simulation conditions tested. However, several caveats apply: the experiments are performed at small scale ( $Q_{\text{red}} \leq 5$ ) using classical simulation; the noise model is simplified; the total gate count per forward

pass is comparable between merged and sequential approaches (Sec. III D); and the 20-step training budget does not probe asymptotic convergence. Validation on actual quantum hardware at larger scale, with hardware-specific noise models and gate-level circuit compilation, remains an important direction for future work, as does extension to more challenging learning tasks where the qubit–execution trade-off may become practically relevant. A systematic comparison with data re-uploading circuits [6] and other qubit-efficient encoding strategies would further clarify the practical advantages of the merged approach.

## ACKNOWLEDGMENTS

The author acknowledges the use of cloud computing resources for the numerical simulations reported in this work.

The data and code that support the findings of this study are available from the corresponding author upon reasonable request.

- 
- [1] J. Biamonte, P. Wittek, N. Pancotti, P. Rebentrost, N. Wiebe, and S. Lloyd, Quantum machine learning, *Nature* **549**, 195 (2017).
- [2] M. Schuld and N. Killoran, Quantum machine learning in feature Hilbert spaces, *Phys. Rev. Lett.* **122**, 040504 (2019).
- [3] M. Cerezo, A. Arrasmith, R. Babbush, S. C. Benjamin, S. Endo, K. Fujii, J. R. McClean, K. Mitarai, X. Yuan, L. Cincio, and P. J. Coles, Variational quantum algorithms, *Nat. Rev. Phys.* **3**, 625 (2021).
- [4] M. Benedetti, E. Lloyd, S. Sack, and M. Fiorentini, Parameterized quantum circuits as machine learning models, *Quantum Sci. Technol.* **4**, 043001 (2019).
- [5] J. Preskill, Quantum computing in the NISQ era and beyond, *Quantum* **2**, 79 (2018).
- [6] A. Pérez-Salinas, A. Cervera-Lierta, E. Gil-Fuster, and J. I. Latorre, Data re-uploading for a universal quantum classifier, *Quantum* **4**, 226 (2020).
- [7] A. N. Kolmogorov, On the representation of continuous functions of many variables by superposition of continuous functions of one variable and addition, *Dokl. Akad. Nauk SSSR* **114**, 953 (1957).
- [8] V. I. Arnold, On functions of three variables, *Dokl. Akad. Nauk SSSR* **114**, 679 (1957).
- [9] Z. Liu, Y. Wang, S. Vaidya, F. Ruehle, J. Halverson, M. Soljacić, T. Y. Hou, and M. Tegmark, KAN: Kolmogorov–Arnold networks, arXiv preprint arXiv:2404.19756 (2024).
- [10] A. Kundu and D. Sarkar, Quantum Kolmogorov–Arnold networks, arXiv preprint arXiv:2410.04435 (2024).
- [11] H. Wakaura, Variational quantum Kolmogorov–Arnold network, Research Square preprint 10.21203/rs.3.rs-5765513/v1 (2024).
- [12] H. Wakaura, Chebyshev-based continuous quantum Kolmogorov–Arnold network, arXiv preprint arXiv:2501.09392 (2025).
- [13] H. Buhrman, R. Cleve, J. Watrous, and R. de Wolf, Quantum fingerprinting, *Phys. Rev. Lett.* **87**, 167902 (2001).
- [14] V. V. Shende, S. S. Bullock, and I. L. Markov, Synthesis of quantum-logic circuits, *IEEE Trans. Comput.-Aided Design Integr. Circuits Syst.* **25**, 1000 (2006).
- [15] D. P. Kingma and J. Ba, Adam: A method for stochastic optimization, Proceedings of the 3rd International Conference on Learning Representations (ICLR) (2015), arXiv:1412.6980.
- [16] F. Wilcoxon, Individual comparisons by ranking methods, *Biom. Bull.* **1**, 80 (1945).
- [17] F. Pedregosa, G. Varoquaux, A. Gramfort, V. Michel, B. Thirion, O. Grisel, M. Blondel, P. Prettenhofer, R. Weiss, V. Dubourg, J. Vanderplas, A. Passos, D. Cournapeau, M. Brucher, M. Perrot, and E. Duchesnay, Scikit-learn: Machine learning in Python, *J. Mach. Learn. Res.* **12**, 2825 (2011).
- [18] S. Wang, E. Fontana, M. Cerezo, K. Sharma, A. Sone, L. Cincio, and P. J. Coles, Noise-induced barren plateaus in variational quantum algorithms, *Nat. Commun.* **12**, 6961 (2021).
- [19] D. Stilck França and R. Garcia-Patron, Limitations of optimization algorithms on noisy quantum devices, *Nat. Phys.* **17**, 1221 (2021).
- [20] J. R. McClean, S. Boixo, V. N. Smelyanskiy, R. Babbush, and H. Neven, Barren plateaus in quantum neural network training landscapes, *Nat. Commun.* **9**, 4812 (2018).
- [21] K. Temme, S. Bravyi, and J. M. Gambetta, Error mitigation for short-depth quantum circuits, *Phys. Rev. Lett.* **119**, 180509 (2017).
- [22] Y. Li and S. C. Benjamin, Efficient variational quantum

- simulator incorporating active error minimization, *Phys. Rev. X* **7**, 021050 (2017).
- [23] M. Kjaergaard, M. E. Schwartz, J. Braumüller, P. Krantz, J. I.-J. Wang, S. Gustavsson, and W. D. Oliver, Superconducting qubits: Current state of play, *Annu. Rev. Condens. Matter Phys.* **11**, 369 (2020).
- [24] K. Mitarai, M. Negoro, M. Kitagawa, and K. Fujii, Quantum circuit learning, *Phys. Rev. A* **98**, 032309 (2018).
- [25] M. Schuld, V. Bergholm, C. Gogolin, J. Izaac, and N. Killoran, Evaluating analytic gradients on quantum hardware, *Phys. Rev. A* **99**, 032331 (2019).